THE JOURNAL OF PHYSICAL CHEMISTRY LETTERS
A JOURNAL OF THE AMERICAN CHEMICAL SOCIETY

pubs.acs.org/JPCL

Letter

Using Hyperoptimized Tensor Networks and First-Principles Electronic Structure to Simulate the Experimental Properties of the Giant {Mn_{84}} Torus

Dian-Teng Chen,[⊥] Phillip Helms,[⊥] Ashlyn R. Hale, Minseong Lee, Chenghan Li, Johnnie Gray, George Christou, Vivien S. Zapf, Garnet Kin-Lic Chan,* and Hai-Ping Cheng*

Cite This: *J. Phys. Chem. Lett.* 2022, 13, 2365−2370

Read Online

ACCESS | Metrics & More | Article Recommendations

ABSTRACT: The single-molecule magnet {Mn_{84}} is a challenge to theory because of its high nuclearity. We directly compute two experimentally accessible observables, the field-dependent magnetization up to 75 T and the temperature-dependent heat capacity, using parameter-free theory. In particular, we use first-principles calculations to derive short- and long-range exchange interactions and compute the exact partition function of the resulting classical Potts and Ising spin models for all 84 Mn $S = 2$ spins to obtain observables. The latter computation is made possible by using hyperoptimized tensor network contractions, a technique developed to simulate quantum supremacy circuits. We also synthesize the magnet and measure its heat capacity and magnetization, observing qualitative agreement between theory and experiment and identifying an unusual bump in the heat capacity and a plateau in the magnetization. Our work also identifies some limitations of current theoretical modeling in large magnets, such as sensitivity to small, long-range exchange couplings.

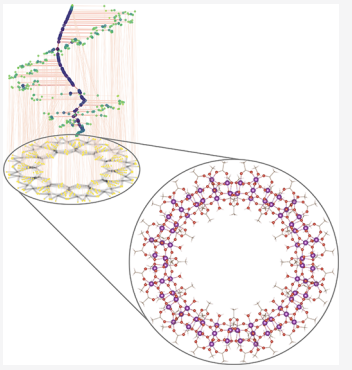

Single-molecule magnets (SMMs) have invoked fascination because of both the possibility to study finite analogues of bulk classical and quantum magnetic phenomena[1] and their potential in information science applications.[2−5] The first SMM $[Mn_{12}O_{12}(O_2CR)_{16}(H_2O)_4]$ was synthesized in the early 1990s, and since then, SMM's of increasing nuclearity have been made.[6−13] In the case of Mn-based SMM's, {Mn_{18}},[10] {Mn_{30}},[11] {Mn_{70}},[12] and {Mn_{84}}[13] have been reported, closing the gap between the largest bottom-up-synthesized SMM and the smallest top-down-synthesized magnetic nanoparticles.[14−16] In fact, the giant {Mn_{84}} torus, first reported in 2004,[13] has an external diameter of 4.3 nm, making it larger than many top-down magnetic nanoparticles.

The large size of these SMMs, with numerous interacting spins, poses interesting challenges to our theoretical understanding. For example, the ground-state spin of {Mn_{84}} is quite small, $S \approx 6$ according to the experimental data,[13] yet there is not an obvious mechanism for how the small nonzero spin arises from the interaction of 84 spins. Furthermore, the spin configuration space in the {Mn_{84}} torus is $5^{84} \approx 5 \times 10^{58}$, exceeding the memory of the largest supercomputers by many orders of magnitude. In previous work, we showed that by using first-principles density functional theory (DFT)-derived exchange couplings, together with a coarse-grained theoretical treatment of the spins, it was possible to uncover the origin of the small but nonzero ground-state spin. In particular, the small long-range exchange couplings renormalize into coarse-grained quadratic spin−spin effective couplings between clusters of spins, breaking the degeneracy of many low-lying spin states and preferentially stabilizing the small nonzero ground-state spin.[17]

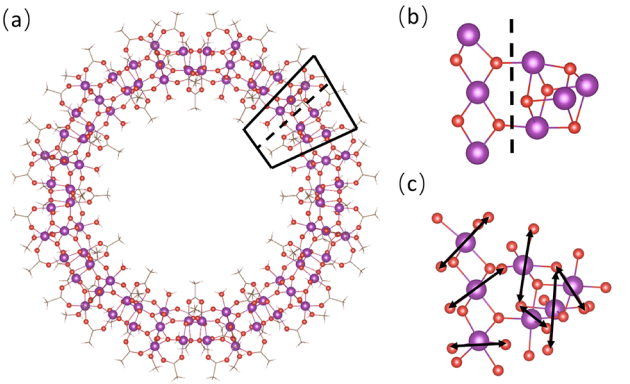

Figure 1. (a) Structure of the {Mn_{84}} torus, with the black box showing (b) the alternating {Mn_3} (linear, left) and {Mn_4} (cubane, right) subunits, separated by the dashed line. (c) Jahn−Teller elongation axes for each Mn^{3+} in the {Mn_7} subunit. Color code: Mn, purple; O, red.

Received: February 5, 2022
Accepted: March 2, 2022
Published: March 7, 2022

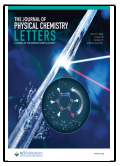

https://doi.org/10.1021/acs.jpclett.2c00354
J. Phys. Chem. Lett. 2022, 13, 2365−2370

In the current work, we extend our previous investigation to report on the theoretical modeling of two directly measurable experimental quantities, namely, the (temperature-dependent) field-dependent magnetization and the heat capacity of the $\{Mn_{84}\}$ torus. We also experimentally measure these quantities, allowing for a direct comparison between theory and experiment in this system. The trajectory of the magnetization with increasing field as it transitions through successive states from $S = 6$ to the saturation magnetization of $344\mu_B$ provides information that constrains the energy scales of the interactions. Here we access part of that phase diagram in high magnetic fields of up to 75 T. Similarly, features in the heat capacity vs temperature plot give insight into the scale of energy gaps between spin states.

Theoretically, our work also demonstrates an *exact* computation of the partition function of 84 $S = 2$ classical spins (in the 5^{84}-dimensional state space). This is made possible by the adaptation of recent exact tensor network contraction methods used to simulate quantum supremacy circuits[18] and demonstrates the power of such techniques beyond quantum circuit settings. We also carry out more extensive first-principles DFT calculations to estimate the long-range exchange couplings. Our work illustrates the state-of-the-art of modeling for the physical properties of the most complicated molecular magnets.

We calculated the electronic energies of the $\{Mn_{84}\}$ torus using Kohn−Sham density functional theory (DFT)[19] with the spin-polarized Perdew−Burke−Ernzerhof (PBE) exchange correlation functional[20] and projector-augmented-wave (PAW) pseudopotentials[21,22] in conjunction with a plane-wave basis (500 eV cutoff energy, energy convergence threshold of 10^{-6} eV) as implemented in the Vienna Ab Initio Simulation Package (VASP).[23,24] We first performed ionic relaxation to obtain the optimized structure of $\{Mn_{84}\}$ until the atomic forces were less than 0.05 eV/Å. Then we used a fixed optimized structure, with a total spin of $S = 4$, to calculate the total energies of different collinear Mn spin configurations.

The DFT energies were fit to a Heisenberg Hamiltonian of the form

$$H_{\text{Heis}} = -\sum_{i<j} J_{ij}\vec{S}_i\cdot\vec{S}_j \tag{1}$$

where $\vec{S}_i$ and $\vec{S}_j$ are $S = 2$ spins (Mn^{3+}) and J_{ij} is their exchange coupling constant. We considered two different Heisenberg exchange models: a short-range 3J model with three nearest-neighbor interactions (Figure 2a) and a long-range 7J model with seven exchange coupling interactions (Figure 2b).

To obtain the finite-temperature field-dependent magnetization and heat capacity, we computed the canonical partition function using tensor network methods. We first made the simplification that the spins are classical spins (which is expected to be qualitatively reasonable from the $1/S$ expansion given the relatively large Mn $S = 2$ spin). We next represented the thermal properties using the five-state Potts model, where each spin is one of five integer values with $S_z \in [-2, -1, 0, 1, 2]$. The energy of the spin configuration in the Potts model is obtained by replacing the vector spins of the Heisenberg model with the integer spins of the Potts model, i.e. (hereon dropping z labels for simplicity),

$$E_{\text{Potts}} = -\sum_{i<j} J_{ij}S_iS_j \tag{2}$$

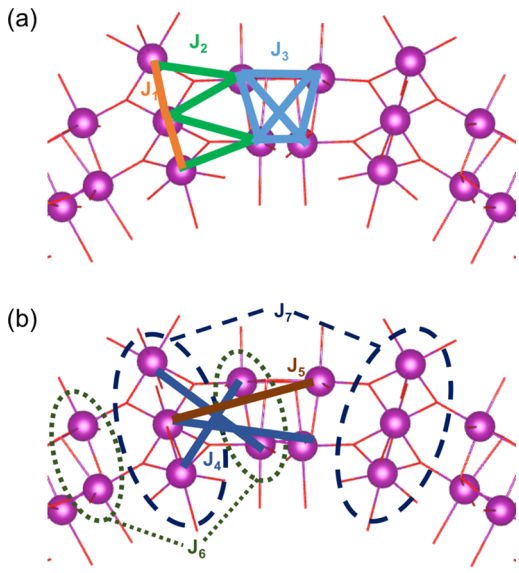

Figure 2. Schematic diagram of the exchange interactions between the Mn^{3+} in $\{Mn_{84}\}$, including (a) nearest-neighbor interactions J_1, J_2, and J_3 and (b) long-range interactions J_4, J_5, J_6, and J_7.

Additionally, to understand the effects of the multiple m_s levels, we performed analogous calculations using an Ising model with $S_z \in [-2, 2]$ and a three-state Potts model with $S_z \in [-2, 0, 2]$.

Even with the above simplifications, the naive computation of the partition function requires a sum over 5^{84} spin configurations

$$Z = \sum_{\{S_i\in(-2,\ldots,2)\}} e^{-\beta E(S_1,S_2,\ldots,S_{84})} \tag{3}$$

where β is inverse temperature and $E(S_1, S_2,..., S_{84})$ is the energy of the classical spin configuration. To evaluate Z, we first re-express the summation exactly as a nested sum of products (a tensor network). This is obtained by using the Boltzmann weights of each pair of spins

$$Z = \sum_{\{S_i\in(-2,\ldots,2)\}} \prod_{i<j} e^{-\beta J_{ij}S_iS_j} \tag{4}$$

We can visualize the above summation structure as a graph (Figure 3) where the nodes represent the Boltzmann weights for a pair of spins from eq 4; each node has two edges, representing the spin indices S_i.

The cost of performing the exact summation (contraction) of such a tensor network is highly dependent on the exact order (contraction path) in which the summation is performed, with most contraction paths being prohibitive in terms of memory or computation time. A similar problem arises in the classical simulation of quantum circuits, which corresponds to a type of large tensor network contraction. Many strategies have been proposed to minimize the cost of such a tensor network contraction by finding the optimal contraction path. To treat the contraction efficiently, we use the software package quimb[25] to construct the tensor network and cotengra[18] to optimize over contraction paths while limiting memory usage and computation cost. The resulting hyperoptimized tensor network contraction path is visualized in Figure 4. To avoid overflow errors encountered during the contraction, the logarithm of the partition function is calculated, with intermediates being stripped of exponentially large or small constants and accounted for after the full contraction. Using this strategy, the exact

https://doi.org/10.1021/acs.jpclett.2c00354
J. Phys. Chem. Lett. 2022, 13, 2365−2370

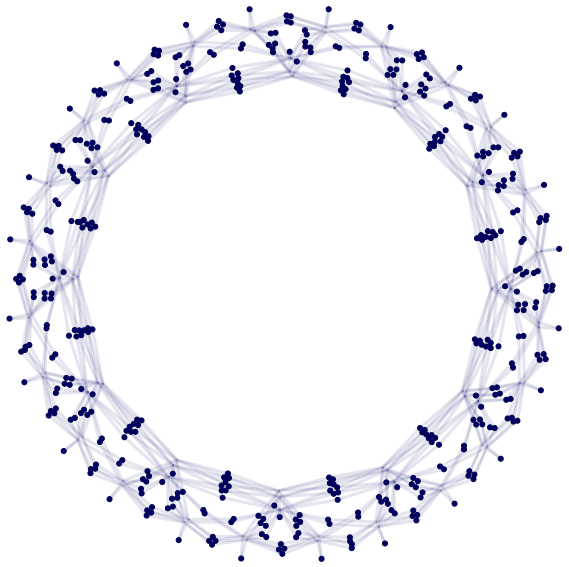

Figure 3. Tensor network representation of the partition function for the classical spin model Hamiltonian.

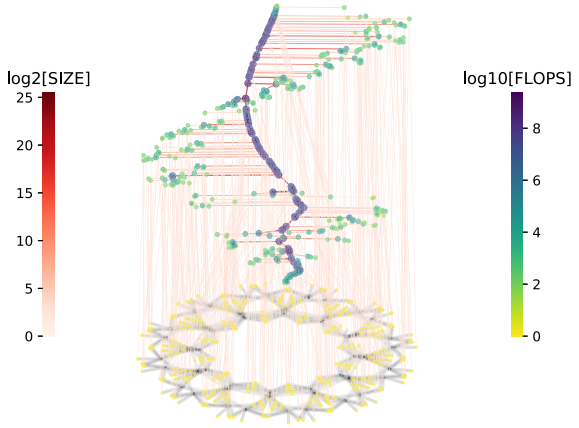

Figure 4. Example contraction tree for the exact contraction of the TN representation of the canonical partition function. The partition function TN is shown on the bottom with yellow transfer matrices and gray indices. Each of the other nodes represents a contraction between tensors, with the color indicating the number of FLOPS required for the contraction. The colored lines indicate which tensors are being contracted, with the color representative of the tensor sizes.

partition function can be computed in a few minutes on a single CPU cluster node.

Given the partition function Z (and thus the free energy $F = -\frac{1}{\beta}\log Z$), we evaluate the magnetization M and heat capacity C_v as the derivatives

$$M = -\frac{\partial F}{\partial B} \tag{5}$$

$$C_v = -\frac{1}{kT^2}\frac{\partial^2 \beta F}{\partial \beta^2} \tag{6}$$

computed numerically with finite difference approximations, where k is Boltzmann's constant, T is temperature, and the magnetic field dependence enters the energy as

$$E(B, \{S_i\}) = E_{\text{Potts}} - \sum_i g\mu_B B S_i \tag{7}$$

where $g = 2.0023$ (atomic units), μ_B is the Bohr magneton, and B is the magnetic field (along the z direction). To isolate the spin contribution to the heat capacity, we also compute the harmonic vibrational contribution to the heat capacity using the GFN-FF force field[26] to carry out a phonon calculation starting from the optimized molecular structures previously obtained by DFT.

Crystalline samples of $\{Mn_{84}Pr\}_{MeOH}$ were prepared according to the published procedure,[13] with the modification that $[Mn_{12}O_{12}(O_2CEt)_{12}(H_2O)_4]$ and $EtCO_2H$ were used as the starting materials, and crystals were isolated after a couple weeks from layering with nitromethane.

Magnetization in millisecond-scale pulsed magnetic fields of up to 60 T was measured on powder samples using the National High Magnetic Field Laboratory's standard approach to pulsed-field magnetization measurements. The measurement coil is a radially compensated coil wound from 50 gauge copper wire. The powder samples were inserted into a nonmagnetic ampule and secured with grease. The coil signal in pulsed fields is proportional to the change in magnetization with time, and the signal is numerically integrated to obtain the magnetization. For each magnetization vs field curve, the ampule in and out of the coil signals under identical conditions were collected, and the ampule-out signal was subtracted from the ampule-in signal to remove background signals. Pulsed-field magnetization data were calibrated with the magnetization data obtained in a vibrating sample magnetometer in a 14 T Physical Properties Measurement System (Quantum Design). The pulsed field was provided by a capacitor-driven 75 T duplex magnet at the National High Magnetic Field Laboratory in Los Alamos.

Using the first-principles procedure described above, we compute the energies of 13 different Ising-like (i.e., each Mn spin is maximally aligned along the z axis, pointing out of the plane of the wheel) spin configurations of $\{Mn_{84}\}$ (Table 1 and Figure 5).

Table 1. Spin Configurations of $\{Mn_{84}\}$[a]

	E (DFT)	E (7J)	E (3J)	total spin
GS1	0	0	0	24
GS2	60.6	60.6	0	0
GS3	90.5	91.5	0	24
GS4	153.7	153.7	0	0
GS5	157.1	155.1	0	12
GS6	217.6	218.6	0	0
RS1	608.4	573.5	496.9	4
RS2	768.2	560.0	519.9	8
RS3	784.8	768.0	654.0	12
RS4	800.3	712.3	601.8	4
RS5	919.9	777.2	692.9	8
RS6	964.1	787.8	800.8	20
FM	4343.7	4610.0	4230.0	168

[a]RS1 to RS6 are random spin configurations that are used to extract nearest-neighbor interactions J_1, J_2, and J_3. GS1 to GS6 are selected degenerate ground-state configurations of the 3J Heisenberg model. The FM configuration has all spins aligned in the same direction (all up or all down). Energies are in meV.

As discussed in ref 17, using only the 3J model (J_1, J_2, and J_3 in Figure 2) results in a large ground-state degeneracy in a classical Ising or Potts model, with ground-state spins of $S = 0$–24. GS1 to GS6 in Table 1 are six of the ground-state spin configurations that would be degenerate within a 3J model. However, as the DFT results show, there is at least a 217.6 meV energy spread

https://doi.org/10.1021/acs.jpclett.2c00354
J. Phys. Chem. Lett. 2022, 13, 2365−2370

Table 2. Exchange Coupling Constants of $\{Mn_{84}\}$ Obtained by Fitting to DFT Energies, for a 3*J* Model (Top Line) and 7*J* Model (Second Line), in meV[a]

	J_1	J_2	J_3	J_4	J_5	J_6	J_7
3*J*	−13.1	−3.3	−1.2				
7*J*	−13.0	−3.2	−1.1	−0.4	1.7	−0.5	−0.8
dist	2.9	3.4	3.1	5.4	5.6	6.5	9.0

[a]Positive values are ferromagnetic couplings, and negative values are antiferromagnetic couplings. The bottom line shows the average distance between the Mn sites for each *J*, in Å.

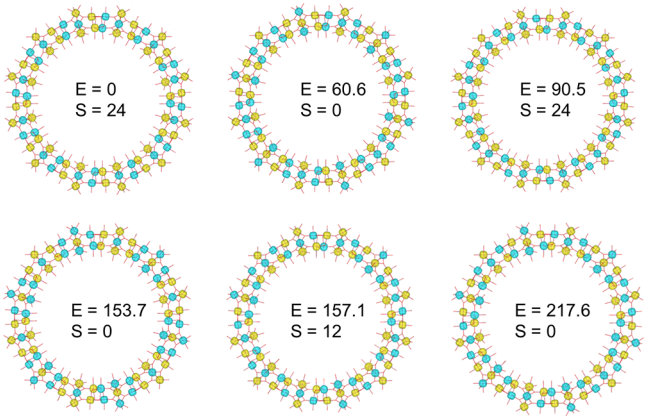

Figure 5. Spin configurations of GS1 to GS6 in Table 1. Yellow represents positive (spin up) and cyan represents negative (spin down). Each Mn^{3+} has a spin of $S = 2$ or −2. The numbers in the center of each spin configuration are the total energy *E* in meV (the lowest one among the six is set to zero) and the total S_z.

between the lowest and highest energies of these "degenerate" states. Thus, the energies are not actually degenerate, presumably because of the longer-range interactions, which are also the interactions that select a specific ground-state spin.

To determine the 3*J* parameters and to estimate the possible long-range exchange couplings, we consider additional configurations RS1−RS6 (randomly chosen) as well as the ferromagnetic configuration FM. We construct a best fit of the 3*J* model to all of these configurational energies. In addition, we introduce long-range interactions, in particular, the J_4−J_7 couplings shown in Figure 2, to model the splitting of the ground-state degeneracy. The results of the fit to the 3*J* and 7*J* models are shown in Table 1; the values of the 3*J* and 7*J* parameters are shown in Table 1. From Table 1 we see that the long-range couplings are all small and alternate in sign, and Table 1 also shows that there are still substantial errors in this fit (e.g., the reversal of the order of RS3 and RS4) reflecting the difficulty in both fitting and perhaps the limitations of the spin Hamiltonian itself. Nonetheless, the main trends are reproduced. We assess the quality of the exchange couplings against experiment in the next section.

As described earlier, starting from an Ising or Potts Hamiltonian using the 3*J* and 7*J* models obtained above, we used hyperoptimized tensor network contraction to calculate the magnetic susceptibility and heat capacity. We now compare the results of this parameter-free theoretical treatment to the experimental measurements.

The theoretical magnetization at 30K is shown in the left panel of Figure 6. The Ising model curves show a clear inflection point occurring for the 3*J* and 7*J* models around $150\mu_B$ and $75\mu_B$, respectively, at magnetization strengths of between 30 and 70 T. The large difference in the vertical magnitude of these curves, however, illustrates the sensitivity to the accuracy of weak long-range exchange couplings. The inflection is reduced as the number of local states increases from the two states of the Ising model to the five-state Potts model.

Experimental magnetization measurements are shown in the right panel of Figure 6 at 0.5 and 30 K. While the lower-temperature curve shows an inflection similar to the Ising model result, the higher-temperature experimental data mirrors the behavior of the Potts models. The experimental magnetization is somewhat smaller in magnitude than results calculated with the 7*J* models and significantly smaller than the 3*J* predictions. Beyond inaccuracies in the long-range exchange couplings highlighted above, another source of discrepancies is the form of the magnetic Hamiltonian: the reduction from the Heisenberg to Potts models, the neglect of magnetic anisotropy, and the alignment of molecules relative to the field in the experimental sample.

The theoretical heat capacity from the spin degrees of freedom is shown in Figure 7, while the total heat capacity (i.e.,

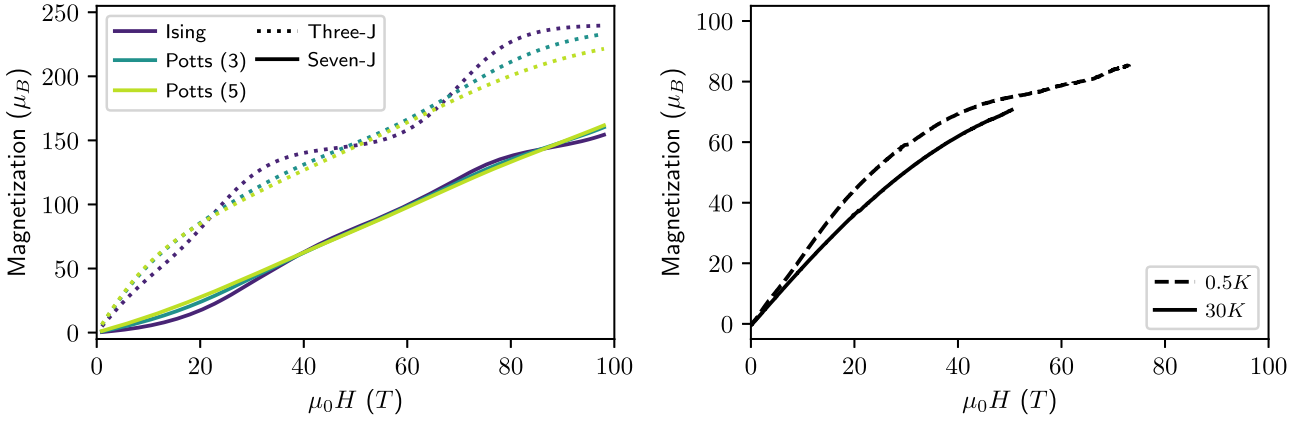

Figure 6. Magnetization of $\{Mn_{84}\}$ as a function of the applied field. The left panel shows the theoretical prediction using the Ising and three- and five-state Potts models and the 7*J* and 3*J* interactions at 30 K, computed using hyperoptimized tensor network contractions. The color of the line corresponds to the spin model used, i.e., an Ising model or a three- or five-state Potts model, and the line style corresponds to whether the long-range (7*J*) or short-range (3*J*) parameters were used. The right panel shows the experimental magnetization curves at 0.5 and 30 K. *H* is the free applied field, and μ_0 is the magnetic permittivity of free space with $B = \mu_0 H$.

https://doi.org/10.1021/acs.jpclett.2c00354
J. Phys. Chem. Lett. 2022, 13, 2365−2370

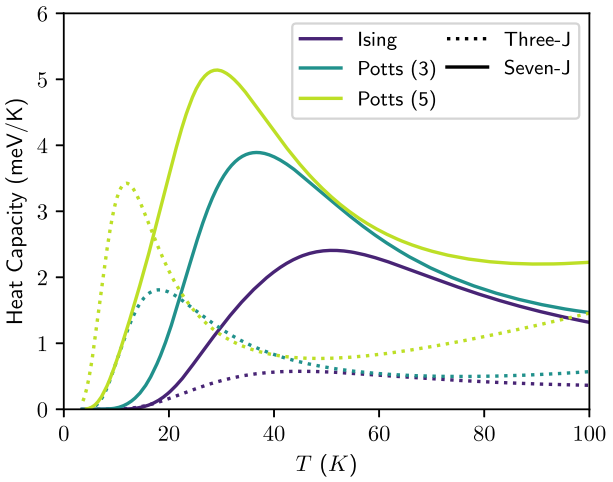

Figure 7. Calculated spin contribution to the heat capacity of $\{Mn_{84}\}$ with the Ising and three- and five-state Potts models, using the 7*J* and 3*J* interactions, with the labeling of curves mimicking what is shown in Figure 6. Results are calculated with no applied magnetic field using hyperoptimized tensor network contractions.

including the contribution of the phonons) is shown together with the experimental heat capacity in Figure 8, both in the absence of a magnetic field. For all models, there are two peaks shown in Figure 7: a sharp one at low temperatures (∼15−60 K) and a broad one at higher temperatures (∼200 K and above, not shown in the figure). The precise temperature at which the peak occurs is strongly model-dependent. The large spin contribution to the heat capacity is manifested as a bump in the total heat capacity when superposed on top of the background phonon contribution. As seen in the right panel of Figure 8, the experimental measured heat capacity shows a bump at around a temperature of nearly 100 K. The bump in the theoretical total heat capacity comes from the first peak in the spin heat capacity, anywhere between 10 and 50 K depending on the model.

In the present work, we carried out theoretical simulations of the giant $\{Mn_{84}\}$ wheel directly targeting two of the common experimental observables used to characterize single-molecule magnets: the heat capacity and the field-dependent magnetic susceptibility. Our theoretical simulations contained no adjustable parameters and featured both large-scale first-principles calculations of the exchange interactions and new hyperoptimized tensor contraction methods for the partition function.

The most interesting features in the observables for $\{Mn_{84}\}$ were the bumps in the heat capacity and the inflection in the field-dependent magnetization, as seen in both theory and experiment. Both must arise from the degeneracy structures we identified previously in the $\{Mn_{84}\}$ energy spectrum. The computed and experimental curves for the heat capacity and magnetization resemble each other, although the energy scales in the computation are shifted from experiment and are very sensitive to fine details in the Hamiltonian. Nonetheless, the qualitatively good agreement illustrates the increasing theoretical capabilities for model low-energy physics even in the most complicated single molecule magnets.

AUTHOR INFORMATION

Corresponding Authors

Garnet Kin-Lic Chan − *Division of Chemistry and Chemical Engineering, California Institute of Technology, Pasadena, California 91125, United States*; Email: gkc1000@gmail.com

Hai-Ping Cheng − *Department of Physics, Center for Molecular Magnetic Quantum Materials and Quantum Theory Project, University of Florida, Gainesville, Florida 32611, United States*; Email: hping@ufl.edu

Authors

Dian-Teng Chen − *Department of Physics, Center for Molecular Magnetic Quantum Materials and Quantum Theory Project, University of Florida, Gainesville, Florida 32611, United States*

Phillip Helms − *Division of Chemistry and Chemical Engineering, California Institute of Technology, Pasadena, California 91125, United States*

Ashlyn R. Hale − *Department of Chemistry, Center for Molecular Magnetic Quantum Materials, University of Florida, Gainesville, Florida 32611, United States*

Minseong Lee − *National High Magnetic Field Laboratory, Los Alamos National Laboratory, Los Alamos, New Mexico 87545, United States*; orcid.org/0000-0002-2369-9913

Chenghan Li − *Division of Chemistry and Chemical Engineering, California Institute of Technology, Pasadena,*

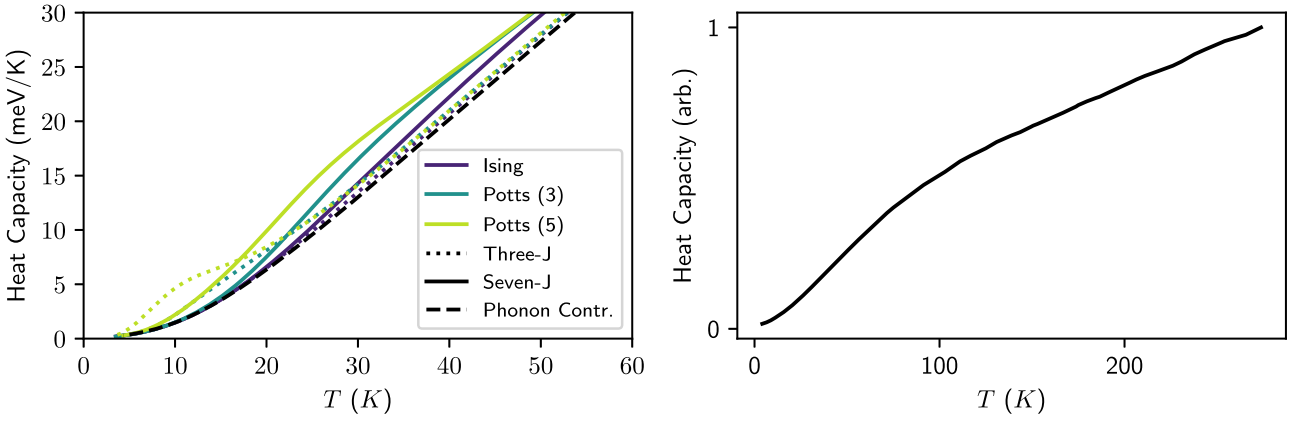

Figure 8. Calculated heat capacity as a function of temperature with no magnetic field. In the left panel, the theoretical prediction is shown, with the phonon contribution to the heat capacity shown as the black dashed line, and the solid and dotted lines include the magnetic contribution computed via the tensor network calculations for the discussed models. The color of these lines refers to the model used, and the line style corresponds to whether long-range (solid) or short-range (dotted) parameters were used. The right panel shows the corresponding experimental curve in arbitrary units.

https://doi.org/10.1021/acs.jpclett.2c00354
J. Phys. Chem. Lett. 2022, 13, 2365−2370

California 91125, United States; orcid.org/0000-0001-6095-9318

Johnnie Gray − *Division of Chemistry and Chemical Engineering, California Institute of Technology, Pasadena, California 91125, United States*

George Christou − *Department of Chemistry, Center for Molecular Magnetic Quantum Materials, University of Florida, Gainesville, Florida 32611, United States;* orcid.org/0000-0001-5923-5523

Vivien S. Zapf − *National High Magnetic Field Laboratory, Los Alamos National Laboratory, Los Alamos, New Mexico 87545, United States;* orcid.org/0000-0002-8375-4515

Complete contact information is available at: https://pubs.acs.org/10.1021/acs.jpclett.2c00354

Author Contributions

⊥D.-T.C. and P.H. contributed equally.

Notes

The authors declare no competing financial interest.

■ ACKNOWLEDGMENTS

Work by D.-T.C., A.R.H., M.L., G.C., V.S.Z., G.K.-L.C., and H.-P.C. was supported by the Center for Molecular Magnetic Quantum Materials, an Energy Frontier Research Center funded by the U.S. Department of Energy, Office of Science, Basic Energy Sciences under award no. DE-SC0019330. C.L. was supported by the U.S. National Science Foundation under award no. 1931328. Support for P.H. was provided by the Simons Investigator program. J.G. was supported by a gift from Amazon Web Services, Inc. The facilities of the National High Magnetic Field Laboratory are funded by the National Science Foundation (cooperative agreement no. DMR-1644779), the Department of Energy, and the State of Florida. Computations were performed at the National Energy Research Scientific Computing Center, at University of Florida Research Computing, and on hardware donated by Nvidia.

■ REFERENCES

(1) Christou, G.; Gatteschi, D.; Hendrickson, D. N.; Sessoli, R. Single-molecule magnets. *MRS Bull.* **2000**, *25*, 66−71.

(2) Friedman, J. R.; Sarachik, M.; Tejada, J.; Ziolo, R. Macroscopic measurement of resonant magnetization tunneling in high-spin molecules. *Physical review letters* **1996**, *76*, 3830.

(3) Thomas, L.; Lionti, F.; Ballou, R.; Gatteschi, D.; Sessoli, R.; Barbara, B. Macroscopic quantum tunnelling of magnetization in a single crystal of nanomagnets. *Nature* **1996**, *383*, 145−147.

(4) Wernsdorfer, W.; Bhaduri, S.; Tiron, R.; Hendrickson, D.; Christou, G. Spin-spin cross relaxation in single-molecule magnets. *Physical review letters* **2002**, *89*, 197201.

(5) Wernsdorfer, W.; Sessoli, R. Quantum phase interference and parity effects in magnetic molecular clusters. *Science* **1999**, *284*, 133−135.

(6) Müller, A.; Krickemeyer, E.; Meyer, J.; Bögge, H.; Peters, F.; Plass, W.; Diemann, E.; Dillinger, S.; Nonnenbruch, F.; Randerath, M.; et al. [Mo154 (NO) 14O420 (OH) 28 (H2O) 70](25 ± 5)-: A Water-Soluble Big Wheel with More than 700 Atoms and a Relative Molecular Mass of About 24000. *Angewandte Chemie International Edition in English* **1995**, *34*, 2122−2124.

(7) Müller, A.; Krickemeyer, E.; Bögge, H.; Schmidtmann, M.; Beugholt, C.; Kögerler, P.; Lu, C. Formation of a Ring-Shaped Reduced "Metal Oxide" with the Simple Composition [(MoO3) 176 (H2O) 80H32]. *Angew. Chem., Int. Ed.* **1998**, *37*, 1220−1223.

(8) Müller, A.; Shah, S. Q.; Bögge, H.; Schmidtmann, M. Molecular growth from a Mo 176 to a Mo 248 cluster. *Nature* **1999**, *397*, 48−50.

(9) Müller, A.; Roy, S. Metal-oxide based nanoobjects: reactivity, building blocks for polymeric structures and structural variety. *Russian chemical reviews* **2002**, *71*, 981.

(10) Brechin, E. K.; Boskovic, C.; Wernsdorfer, W.; Yoo, J.; Yamaguchi, A.; Sanudo, E. C.; Concolino, T. R.; Rheingold, A. L.; Ishimoto, H.; Hendrickson, D. N.; et al. Quantum tunneling of magnetization in a new [Mn18] 2+ single-molecule magnet with S= 13. *J. Am. Chem. Soc.* **2002**, *124*, 9710−9711.

(11) Soler, M.; Rumberger, E.; Folting, K.; Hendrickson, D. N.; Christou, G. Synthesis, characterization and magnetic properties of [Mn30O24 (OH) 8 (O2CCH2C (CH3) 3) 32 (H2O) 2 (CH3NO2) 4]: the largest manganese carboxylate cluster. *Polyhedron* **2001**, *20*, 1365−1369.

(12) Vinslava, A.; Tasiopoulos, A. J.; Wernsdorfer, W.; Abboud, K. A.; Christou, G. Molecules at the quantum−classical nanoparticle interface: giant Mn70 single-molecule magnets of 4 nm diameter. *Inorganic chemistry* **2016**, *55*, 3419−3430.

(13) Tasiopoulos, A. J.; Vinslava, A.; Wernsdorfer, W.; Abboud, K. A.; Christou, G. Giant Single-Molecule Magnets: A {Mn84} Torus and Its Supramolecular Nanotubes. *Angew. Chem.* **2004**, *116*, 2169−2173.

(14) Batlle, X.; Labarta, A. Finite-size effects in fine particles: magnetic and transport properties. *Journal of Physics-London-D Applied Physics* **2002**, *35*, 201.

(15) Hyeon, T. Chemical synthesis of magnetic nanoparticles. *Chem. Commun.* **2003**, 927−934.

(16) Laurent, S.; Forge, D.; Port, M.; Roch, A.; Robic, C.; Vander Elst, L.; Muller, R. N. Magnetic iron oxide nanoparticles: synthesis, stabilization, vectorization, physicochemical characterizations, and biological applications. *Chem. Rev.* **2008**, *108*, 2064−2110.

(17) Schurkus, H. F.; Chen, D.; O'Rourke, M. J.; Cheng, H.-P.; Chan, G. K.-L. Exploring the Magnetic Properties of the Largest Single-Molecule Magnets. *journal of physical chemistry letters* **2020**, *11*, 3789−3795.

(18) Gray, J.; Kourtis, S. Hyper-optimized tensor network contraction. *Quantum* **2021**, *5*, 410.

(19) Kohn, W.; Sham, L. J. Self-consistent equations including exchange and correlation effects. *Physical review* **1965**, *140*, A1133.

(20) Perdew, J. P.; Burke, K.; Ernzerhof, M. Generalized gradient approximation made simple. *Physical review letters* **1996**, *77*, 3865.

(21) Blöchl, P. E. Projector augmented-wave method. *Phys. Rev. B* **1994**, *50*, 17953.

(22) Kresse, G.; Joubert, D. From ultrasoft pseudopotentials to the projector augmented-wave method. *Phys. Rev. B* **1999**, *59*, 1758.

(23) Kresse, G.; Furthmüller, J. Efficiency of ab-initio total energy calculations for metals and semiconductors using a plane-wave basis set. *Computational materials science* **1996**, *6*, 15−50.

(24) Kresse, G.; Furthmüller, J. Efficient iterative schemes for ab initio total-energy calculations using a plane-wave basis set. *Phys. Rev. B* **1996**, *54*, 11169.

(25) Gray, J. quimb: A python package for quantum information and many-body calculations. *Journal of Open Source Software* **2018**, *3*, 819.

(26) Spicher, S.; Grimme, S. Robust atomistic modeling of materials, organometallic, and biochemical systems. *Angew. Chem.* **2020**, *132*, 15795−15803.